Journal of Power Sources 603 (2024) 234401

Contents lists available at ScienceDirect

Journal of Power Sources

journal homepage: www.elsevier.com/locate/jpowsour

Deep neural network-based modeling and optimization methodology of fuel cell electric vehicles considering power sources and electric motors

Dong-Min Kim [a], Kihan Kwon [b], Kyoung-Soo Cha [c], Seungjae Min [d], Myung-Seop Lim [d,*]

[a] Department of Automotive Engineering, Honam University, Gwangju, 62399, Republic of Korea
[b] Department of Mechanical Design Engineering, Jeonbuk National University, Jeonju, 54896, Republic of Korea
[c] Mobility System R&D Group, Korea Institute of Industrial Technology, Daegu, 42994, Republic of Korea
[d] Department of Automotive Engineering, Hanyang University, Seoul, 04763, Republic of Korea

GRAPHICAL ABSTRACT

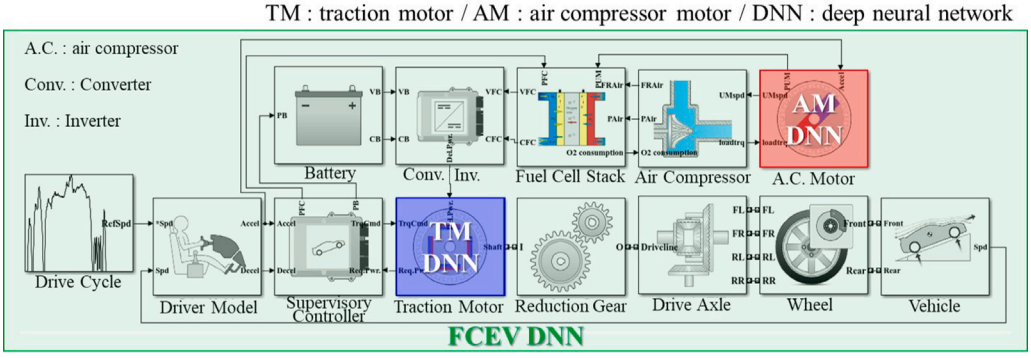

HIGHLIGHTS

- Detailed modeling of the fuel cell electric vehicle was performed.
- Wide variation of DC link voltage due to fuel cell characteristics was considered.
- Effect of the air supply system on fuel cell performance was reflected.
- Adoptive layering and sampling algorithm for deep neural network was suggested.

ARTICLE INFO

Keywords:
Adaptive layering and sampling (ALS)
Air compressor motor
Deep neural network
Energy consumption
Fuel cell electric vehicle (FCEV)
Traction motor

ABSTRACT

This study proposes a modeling and optimization methodology for fuel cell electric vehicles (FCEVs). Among FCEV components, the traction motor, lithium-ion battery, fuel cell stack, and air supply system are mainly investigated. The FCEV modeling is performed based on the vehicle specifications, electromagnetic finite element analysis, and experimental data. To conduct design optimization, deep neural networks (DNNs) are adopted and trained to predict vehicle performance considering the fluctuation of applied direct current voltage. At this stage, the adaptive layering and sampling algorithm was suggested, which enables efficient DNN construction. To confirm the feasibility of the suggested training algorithm, the number of hidden layers and sampling points of constructed DNNs are investigated. Finally, DNN-based fuel economy optimization is performed considering the driving performance. The effectiveness of the proposed optimization methodology is validated by additional optimization results.

* Corresponding author.
E-mail address: myungseop@hanyang.ac.kr (M.-S. Lim).

https://doi.org/10.1016/j.jpowsour.2024.234401
Received 23 November 2023; Received in revised form 11 February 2024; Accepted 19 March 2024
Available online 27 March 2024

1. Introduction

Following the Paris Agreement, efforts to reduce greenhouse gas (GHG) emissions have increased worldwide [1]. Moreover, several commercial vehicle manufacturers have planned to stop the production of pure internal combustion engine (ICE) vehicles [2]. Based on this GHG mitigation tendency, fuel cell electric vehicles (FCEVs) are treated as candidates for future eco-friendly mobility [3,4]. This basis originates from the fact that FCEVs purify air and emit pure water. In addition, FCEVs account for less refueling time and exhibit superior driving range compared with battery electric vehicles (BEVs)

In recent times, the commercialization of FCEVs has been driven by several countries. However, several obstacles need to be addressed. The representative impediments are refueling stations, cost, durability, and performance of FCEV [5]. Among them, performance and convenience play important roles in the mass production of FCEVs. Therefore, performance improvement is one of the crucial aspects that need to be solved.

As listed in Table 1, the literature survey has been previously conducted to set the direction of this study. This survey included papers published after 2016, and the topics were xEV design and optimization. More than half of the studies adopted a sizing method to optimize vehicles [6–14]. There are two categories of sizing. One category sizes the powertrain and source simultaneously [6–10], whereas the other category sizes power source only [11–14]. Moreover, studies on FCEVs were conducted based on FC stack and battery sizing [9–14]. Furthermore, studies on topology change play a major factor [15–18]. In the case of EV design, multi-motor methodology is mainly selected [15–17]. In addition, vehicle design based on electric motor geometry optimization [19,20] and winding connection changes [21] exist.

However, [6,19,21] well considered the electric motor characteristics based on the electromagnetic finite element analysis (FEA). Although several studies on the air compressor motors of FCEVs have been conducted [22–25], the design process for FCEVs has not been considered. Moreover, the fluctuation characteristics of the output voltage of the FC stack have not been reflected.

Prior concerns for improving the performance of an FCEV are reduction in weight and increase in power density of the fuel cell stack need to be prioritized. For this objective, oxygen at a higher flow rate and higher pressure should be supplied to the stack [26,27]. Accordingly, the output power and rotation speed of the air compressor driver electric motor should be increased. Therefore, the air supply system including the air compressor motor should be considered as the main component in the FCEV design process. Moreover, the output voltage of the FC exhibits a wide variation range [28,29]. Therefore, wide voltage fluctuations should be considered to estimate the performance of the traction and air compressor motors.

This study suggests the modeling and optimization methodology of FCEVs considering the air supply system for the FC stack and polarization characteristics of the FC stack. The performance of the air compressor has been considered in FC stack performance. Furthermore, the wide variation in the DC link voltage (FC stack output voltage) is considered while estimating the performance of electric motors. In this process, deep neural networks (DNNs) are constructed to reduce the computation time. For efficient DNN generation, an adaptive layering and sampling (ALS) algorithm is proposed. The contributions of this study can be summarized as follows:

- The detailed modeling of the fuel cell electric vehicle was performed.
- The wide variation of DC link voltage caused by fuel cell stack characteristics was considered.
- The air supply system for the proton exchange membrane fuel cell stack was reflected.
- The adoptive layering and sampling algorithm for deep neural network construction was suggested.

The study comprises modeling, neural network training, and optimization and is organized as follows: First, specifications and relevant information are introduced. Second, electric powertrain modeling based on electromagnetic FEA is presented. Third, the hybrid modeling of the air supply system is performed based on the real and computer-based experimental results. In the last stage of the modeling process, the lithium-ion battery and FC stack are modeled. The proposed ALS algorithm is explained for neural network construction. Using this algorithm, the electric motor performance surrogate modeling based on the size of the electric motors and DC link voltages is conducted for the traction and air compressor motors. These electric-motor DNNs were implanted to the FCEV simulation model. Fourth, using this simulation model, the FCEV trace performance analysis and fuel economy surrogate modeling based on the sizing of the two electric motors are performed. Finally, based on the FCEV DNNs, the fuel economy optimization of FCEV is achieved.

2. Method part 1: FCEV modeling

This part explains the proposed FCEV modeling methodology. As shown in Figure S1, utilizing MATLAB Simulink, an FCEV was modeled. The driver model, reduction gear, drive axle, wheel, and vehicle block were adopted from the Powertrain Blockset of Simulink. The FC stack was considered as a detailed version from the Simscape library; this version can exhibit oxygen flow. Other parts, e.g., supervisory controller, battery, converter, inverter, air compressor, and air compressor motor, were modeled using a customized process. A supervisory controller block was modeled to control traction and air compressor motors. In addition, the power and energy management for the battery and FC stack plays an important role. Sections 2.1–2.3 explain the electric powertrain, air supply system, and power sources.

The target vehicle of this study is Hyundai NEXO, which is a mid-sized sports utility vehicle. The specifications are listed in Table 2 [30]. They are based on a 17-inch wheel-equipped condition. Then, the vehicle, drive axle, and wheel were modeled. In particular, government-certified standard fuel efficiency allowed the FCEV model to reflect unknown losses.

Table 3 lists the brief specifications of the main components of the FCEV [31]. The configuration is estimated from the input and output voltages of power electronic devices and power sources. The level of the bidirectional DC/DC converter input voltage includes the rated battery voltage. Therefore, it was inferred that the input terminal of the bidirectional DC/DC converter is connected to the battery. The range of the battery output voltage is estimated to be the same as that of the bidirectional DC/DC converter input voltage. Conversely, the output voltage of the bidirectional DC/DC converter was the same as that of the FC stack. Accordingly, it is assumed that the bidirectional DC/DC converter would convert the battery voltage to the FC stack voltage. In addition, it can be assumed that the converter-equipped battery is connected parallel to the FC stack. Consequently, this study modeled this terminal as the DC link voltage with regard to the inverter of electric motors.

2.1. Electric powertrain

The electric powertrain includes a single reduction gear and an electric traction motor. This section demonstrates the performance calculation of the electric traction motor and the modeling process. Table 4 lists the specifications of the electric traction motor. We considered 8 poles and 48 slots, which are widely used for EV traction. The maximum speed was inversely calculated based on the wheel size, reduction gear ratio, and maximum vehicle speed. The derived relationship is expressed in Eq. (1), where N_{MAX} is the maximum rotational speed of the motor (rpm), n_g is the reduction gear ratio, r_w is the wheel radius of the tire (m), and V_{MAX} is the vehicle maximum speed (m/s).

Table 1
Previous study on vehicle design and optimization based on component sizing.

Method		Target	Design variable	Vehicle model	Motor model	Ref.
Sizing	Overall sizing	HEV	*EM.L*$_{stk}$, n_g, *Batt.P*, *Gen.P*	1D model	FEA based	[6]
		HEV	*EM.P*, *Batt.Ns*, *Batt.Np*	1D model	EMC based	[7]
		HEV	*EM.P*, n_g, *ICE.P* *Batt.Ns*, *Batt.Np* *SC.Ns*, *SC.Np*	1D model	Omitted	[8]
		FCEV	*EM.T*, *Batt.P*,*FC.P*	1D model	Assumption	[9]
		FCEV	*EM.T*, *Batt.P*,*FC.P*	1D model	Assumption	[10]
	Source sizing	FCEV	*Batt.P*, *FC.P*	Equation	Omitted	[11]
		FCEV	*Batt.P*, *FC.P*	Driving data	Omitted	[12]
		FCEV	*Batt.P*, *FC.P*	1D model	Assumption	[13]
		FCEV	*Ref.P*, *Batt.P*, *FC.P*	Equation	Assumption	[14]
Electric motor optimization		EV	*EM.Geometries*	Equation	FEA based	[19]
		EV	*EM.Geometries*	Equation	Equation	[20]
Layout change	Dual motor	EV	T_1, T_2, n_{g1}, n_{g2}	1D model	Assumption	[15]
		EV	T_1, T_2, n_{g1}, n_{g2}	Equation	Equation	[16]
	Multimotor	EV	N_{EM}, $EM_S.T$, $EM_S.S$	Equation	Equation	[17]
	Config.	HEV	*EMs.P*, $n_g s$, *ICE.P*	1D Model	Assumption	[18]
Winding changeover		EV	*N1 : N2*	1D model	FEA based	[21]

Table 2
Specification of the target fuel cell electric vehicle.

Items		Value	Unit
Drag coefficient		0.329	–
Driving system		Front-wheel driving	–
Empty vehicle weight		1820	kg
Government -certified standard fuel efficiency	Combined	2.86	km/kWh
	City	2.96	km/kWh
	Highway	2.76	km/kWh
Maximum speed		177	km/h
Overall length		4670	mm
Overall width		1860	mm
Overall height		1630	mm
Wheel diameter		432	mm

$$N_{MAX} = \frac{n_g \times 60}{2\pi r_w} \times V_{MAX} \quad (1)$$

The nominal DC voltage was assumed based on the average value of the voltage–power curve of the FC stack. Permanent magnets and electrical steel sheets are widely used in EV traction motor production. The rotor type adopted was the second layer V-type, which is commonly used. The estimated cross-sectional area of the electric traction motor is shown in Figure S2. Based on the cross-sectional area and these conditions, the size and number of armature turns were estimated to satisfy the maximum output power range and maximum speed. This process was conducted using an electromagnetic FEA.

Based on the determined electric motor geometries, the performance evaluation process was performed (Figure S3) [32]. Utilizing electromagnetic FEA, the lumped parameters, i.e., *d*- and *q*-axis inductances L_d and L_q, linkage flux Ψ_a, and iron loss were first calculated for various input-current conditions. Then, considering the DC link voltage,

Table 3
Specifications of the main components.

Items		Value	Unit
Electric powertrain	Motor type	IPMSM	–
	Motor maximum output	113	kW
	Motor maximum torque	395	Nm
	Reduction gear ratio	7.981:1	–
Inverter	Input voltage	240–450	V
Bidirectional DC/DC converter	Input voltage	160–275.2	V
	Output voltage	250–450	V
Fuel cell stack	Maximum output power	95	kW
	Output voltage	250–450	V
Battery	Type	Li-ion polymer	–
	Rated voltage	240	V
	Capacity	6.5	Ah
	Energy	1.56	kWh
	Weight	51.2	kg
Fuel tank	Capacity	156.6	L

Table 4
Specifications of the electric traction motor.

Items	Value	Unit	Note
Pole/Slot number	8/48	–	–
Maximum output power	113	kW	@3000–4600 rpm
Maximum torque	395	N m	–
Maximum speed	10600	rpm	Assumption
Nominal DC voltage	280	V	based on
Maximum current	449.7	A_{rms}	specification
Maximum current density	22.6	A_{rms}/mm^2	

the MTPA current was determined based on the *d*-*q* equivalent circuit according to Eqs. (2)–(4), where R_a is the armature winding resistance, R_I is the equivalent iron loss resistance, v_d is the *d*-axis voltage, and v_q is the *q*-axis voltage. v_{od} and v_{oq} are the induced voltages of the

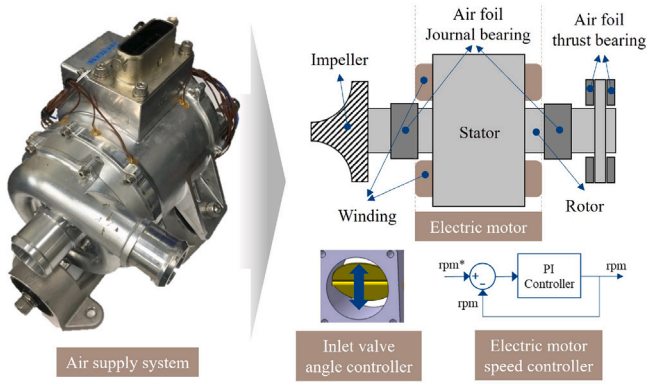

Fig. 1. Configuration of air supply system for FC stack.

Table 5
Specifications of the air compressor motor.

Items	Value	Unit	Note
Pole/Slot number	2/6	–	–
Maximum output power	10	kW	@100000 rpm
Maximum torque	0.96	N m	–
Maximum speed	100000	rpm	–
Nominal DC voltage	280	V	Same as traction motor
Maximum current	48.2	A_{rms}	–
Maximum current density	8.5	A_{rms}/mm^2	–

d and q axes, respectively, and ω indicates the electrical rotational angular speed. i_d and i_q are the armature currents of the d and q axes, respectively. i_{od} and i_{oq} are the iron loss-subtracted values of the d- and q-axis currents, respectively, which are obtained from the equivalent iron loss resistance. Finally, in addition to the torque T and speed condition, an efficiency map was generated using Eq. (5).

$$\begin{bmatrix} v_d \\ v_q \end{bmatrix} = R_a \begin{bmatrix} i_{od} \\ i_{oq} \end{bmatrix} + \left(1 + \frac{R_a}{R_I}\right) \begin{bmatrix} v_{od} \\ v_{oq} \end{bmatrix} + p \begin{bmatrix} L_d & 0 \\ 0 & L_q \end{bmatrix} \begin{bmatrix} i_{od} \\ i_{oq} \end{bmatrix}$$
$$\begin{bmatrix} v_{od} \\ v_{oq} \end{bmatrix} = \begin{bmatrix} 0 & -\omega L_q \\ \omega L_d & 0 \end{bmatrix} \begin{bmatrix} i_d \\ i_q \end{bmatrix} + \begin{bmatrix} 0 \\ \omega \Psi_a \end{bmatrix} \quad (2)$$

$$T = P_p \left\{ \Psi_a i_{oq} + \left(L_d - L_q\right) i_{od} i_{oq} \right\} \quad (3)$$

$$W_C = R_a \left(i_d^2 + i_q^2 \right) \quad (4)$$

$$\eta_{em} = \frac{\omega_m T}{\omega_m T + W_C + W_I} \quad (5)$$

2.2. Air supply system

The performance of the air compressor is considered for the air supply system. As shown in Fig. 1, the air compressor comprised an electric motor, inlet valve angle controller, and electric motor speed controller. In the electric motor part, an impeller to compress the input air is connected to the rotor of the electric motor. In addition, thrust runners, thrust bearings, and journal bearings are installed. The performance of the electric motor was analyzed based on the electric traction motor mechanism, without considering the rotor loss calculation. The other parts were considered based on the experimental results.

To estimate the performance of the air compressor motor, the cross-sectional area, as shown in Figure S4, was used. The specifications of the air compressor motor are listed in Table 5. Based on the geometry and specifications, the performance of the air compressor motor was calculated using the same calculation process as that of the traction motor, as explained in Section 2.1. However, unlike traction motors, air compressor motors possess retaining sleeves that conduct eddy currents. In addition, the operating rotational speed is very high.

Table 6
Polynomial fitting evidence with regard to the performance of the air compressor.

Fitting equation	Goodness of fit	Value		
		Airflow rate	Air pressure	Load torque
2nd order	R-squared	0.9996	0.9987	0.9986
	RMSE	1.597	0.009233	0.00682
3rd order	R-squared	0.9999	0.9997	0.9992
	RMSE	0.9871	0.004833	0.005282
4th order	R-squared	0.9999	0.9997	0.9992
	RMSE	0.7626	0.004916	0.005486
5th order	R-squared	0.9999	−7.102	−38.21
	RMSE	0.7136	0.7967	1.263
6th order	R-squared	0.9999	−27630000	−508200000
	RMSE	0.7572	1552	4795

Therefore, an air compressor motor experiences a large eddy current loss [33].

To precisely consider the eddy current loss to predict the motor performance, 3D FEA should be performed in addition to other analyses. However, the calculation of eddy current loss using 3D FEA for all the predicted operating points is time-consuming. To overcome this high computation time, the eddy current loss estimation process was adopted (Figure S5) [34].

Subsequently, the test-oriented compression performance modeling was achieved. As shown in Fig. 2, the experimental setup was prepared. Using this test bench, the air pressure and flow rate were measured at various electric motor speeds and inlet valve angles.

Based on the test results of the air compressor, the empirical models were generated to analyze the compression performance. The generated models are illustrated in Figure S6. The surfaces indicate derived models, and the spheres indicate measured points or estimates from the measured points. These surfaces originated from the polynomial fitting of the spheres. The polynomial order of each model was determined based on the goodness of fit. The coefficient of determination (R^2) and root mean square error (RMSE) were adopted as the goodness of fit parameters. For the airflow rate, air pressure, and load torque, the fifth, third, and third polynomial orders were determined, respectively. The polynomial fitting results are listed in Table 6.

2.3. Power sources

In this study, the power sources of the FCEV include a PEMFC and lithium-ion battery. The PEMFC is the main source, and the lithium-ion battery is the auxiliary source.

For the PEMFC modeling, the equivalent circuit suggested by Larminie and Dicks was adopted [35]. The model is illustrated in Fig. 3. The detailed model in the MATLAB Simulink library was used to demonstrate the performance of the air supply system. The corresponding equations are expressed as Eqs. (6)–(14) [36].

$$E = E_{oc} - NA \ln\left(\frac{i_{fc}}{i_0}\right) \cdot \frac{1}{sT_d/3 + 1} \quad (6)$$

$$V_{fc} = E - R_{ohm} \cdot i_{fc} \quad (7)$$

$$E_{oc} = K_c \cdot E_n \quad (8)$$

$$i_0 = \frac{zFk\left(P_{H_2} + P_{O_2}\right)}{Rh} \cdot \exp\left(\frac{-\Delta G}{RT}\right) \quad (9)$$

$$A = \frac{RT}{Z\alpha F} \quad (10)$$

$$Uf_{H_2} = \frac{60000RTi_{fc}}{zFP_{fuel}V_{fuel}x\%} \quad (11)$$

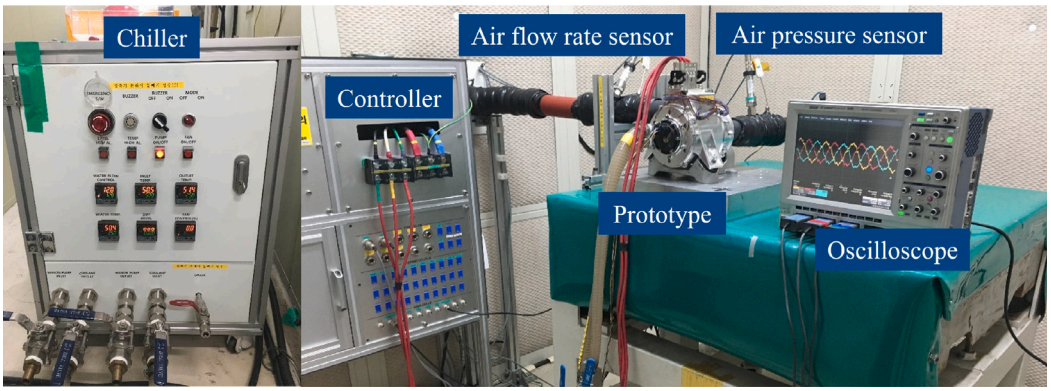

Fig. 2. Air compressor test bench.

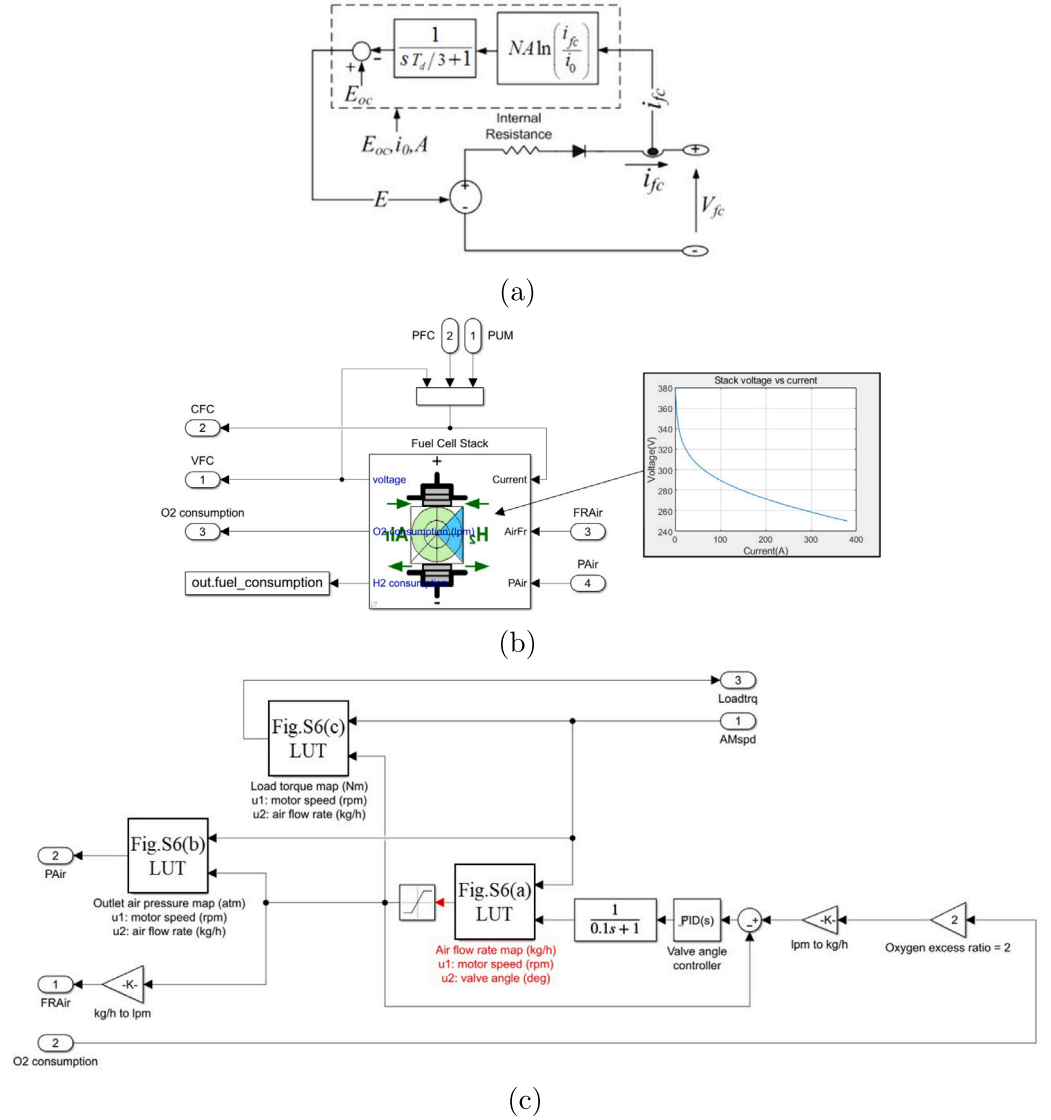

Fig. 3. Proton membrane exchange fuel cell model (a) equivalent circuit, (b) fuel cell modeling, (c) air supply system modeling.

$$Uf_{O_2} = \frac{60000RTi_{fc}}{2zFP_{air}V_{air}y\%} \tag{12}$$

$$P_{H_2} = \left(1 - Uf_{H_2}\right)x\%P_{fuel} \tag{13}$$

$$P_{O_2} = \left(1 - Uf_{O_2}\right)y\%P_{air} \tag{14}$$

Here, A denotes the Tafel slope; E_n and E_{oc} denote the Nernst and open-circuit voltage, respectively; h is Planck's constant; i_0 and i_{fc} denote the exchange and FC currents, respectively; k and K_c denote

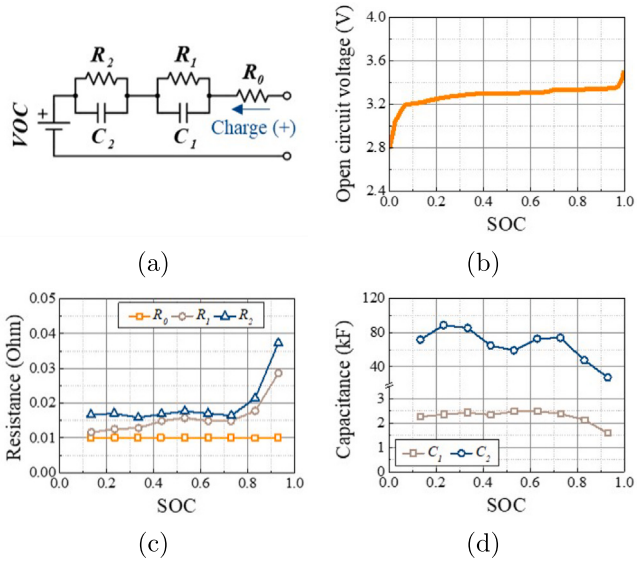

Fig. 4. Lithium-ion battery model (a) equivalent circuit, (b) open-circuit voltage, (c) resistance, (d) capacitance.

Boltzmann's constant and voltage constant, respectively; P_{air} and P_{fuel} denote the absolute supply pressures of air and fuel, respectively; P_{O_2} and P_{H_2} denote the partial pressures of oxygen and hydrogen insider stack, respectively; R_{ohm} is the internal resistance; T and T_d denote the operating temperature and response time, respectively; Uf_{O_2} and Uf_{H_2} denote the utilization rates of hydrogen and oxygen, respectively; V_{air}, V_{fuel}, and V_{fc} denote the flow rates of air, fuel, and FC voltage, respectively; x and y denote the percentages of hydrogen and oxygen in fuel and air, respectively; z is the number of moving electrons; α is the charge transfer coefficient; ΔG is the activation energy barrier. The oxygen excess ratio, which indicates the supplied oxygen ratio compared with the oxygen consumption ratio, was assumed to be 2. This constant control setup can achieve the normal performance of the FC stack [37–39].

In the case of lithium-ion battery modeling, a second-order R-C paired equivalent circuit was adopted to reflect the consecutive charge/discharge situations that occur in real driving conditions. The equivalent circuit and corresponding coefficients are shown in Fig. 4 [40,41].

2.4. Energy management

The energy management strategy was estimated from real driving data. The real driving data was measured from actual driving FCEV driven as a drive cycle as shown in Figure S7. First, a rule-based energy-management strategy was developed. The SOC of lithium-ion battery and output power request, EV mode, FC mode, and hybrid source modes were designed. The EV and FC modes represent the battery-only and FC-only modes, respectively. In the H1 mode, the FC charges the battery and drives the vehicle simultaneously, whereas in the H2 and H3 modes, the FC and battery drive the vehicle. In the H2 mode, the FC is operated at the upper boundary of the efficient region, and the battery is operated to assist the remaining required power. In the H3 mode, the battery is operated at maximum power, and the FC is operated at the remaining required power. This strategy is illustrated in Fig. 5.

Then, the thresholds of the energy management strategy were optimized to minimize the difference between the simulated and real driving data. The normalized RMSE (NRMSE) of the simulation and real driving data was set as the objective function and minimized.

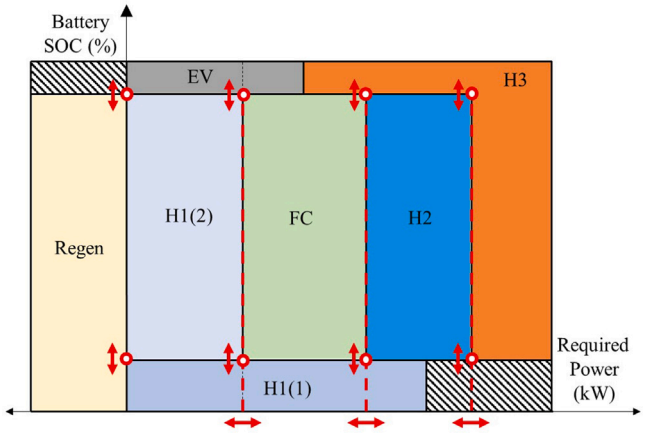

Fig. 5. Rule-based energy management strategy.

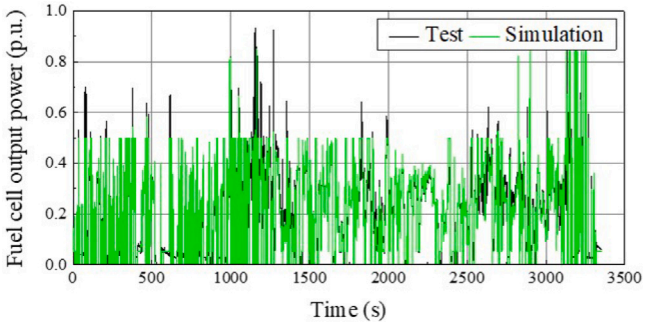

Fig. 6. Comparison of the FC output profiles based on the test and simulation results.

The normalized FC output profiles of the simulation and real data are compared in Fig. 6.

However, there are still some errors between the results of the test and the simulation. This occurs since the real driving test was conducted in the valley area, which can be recognized from Figure S7 (b). This valley condition included the fluctuation of atmosphere pressure. In addition, the performance of the fuel cell stack is dependent on ambient pressure [42]. Therefore, the consideration of ambient pressure change in this simulation is hard, and this remained a limitation of this study.

3. Method part 2: FCEV optimization

This part introduces the deep neural network (DNN) construction and design problem formulation. The DNN was adopted to conduct FCEV optimization using the modeled FCEV, as described in Section 2. This process was performed based on the MATLAB neural network toolbox [43]. The Sigmoid function was used as the activation function, and the Bayesian regularization algorithm was used for back-propagation. The numbers of sampling points and hidden layers were adaptively determined, and this process is explained in Section 3.1. Using the proposed algorithm, the DNNs of the electric motors and FCEV were constructed. Finally, the design formulation for FCEV fuel economy optimization was presented.

3.1. Adaptive layering and sampling algorithm

To efficiently construct the DNN, the ALS algorithm was suggested (Figure S7 in supplementary materials). This algorithm allows the DNN structure to differ according to the regression value of the test set R_{Test}. Initial sampling was conducted based on optimal Latin hypercube

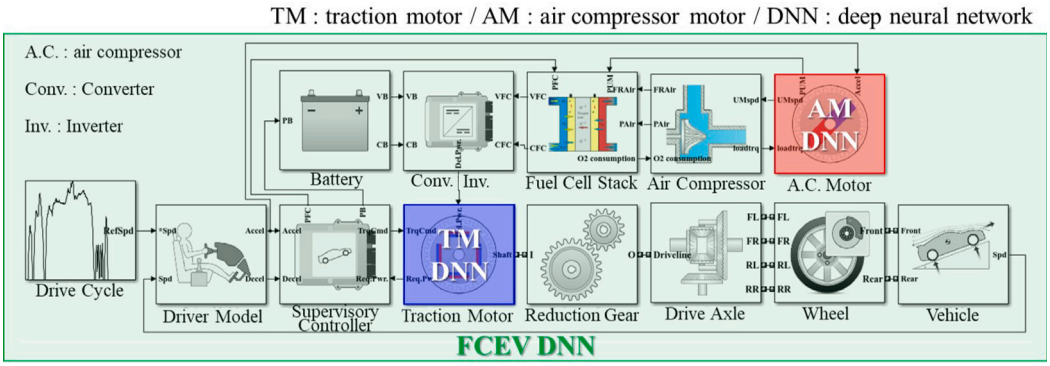

Fig. 7. Construction of fuel cell electric vehicle network.

sampling (OLHS), and additional sampling was performed based on maximin distance sampling (MDS) [44,45]. Subsequently, according to the R_{Test} variation, additional sampling and layering were performed. Finally, if the R_{Test} value was successively greater than 0.99, the DNN construction was completed. In addition, the sampling points for this process were determined using Eq. (15).

$$N_s = \begin{cases} 10 \times n_v, & \text{if } s = 1 \\ 0, & \text{otherwise } s = 2, 3, 4, \ldots \end{cases} \tag{15}$$

3.2. Electric motor networks

The electric motor DNNs were constructed for the traction and air compressor motors. The trained responses included the maximum torque and total loss. The maximum torque was estimated according to the number of armature turns, stack length of the motor, DC link voltage, and motor speed. The total loss was estimated under the same conditions set for the maximum torque estimation, along with the output torque. The range of the conditions was determined based on electrical and mechanical limits. In particular, the maximum speed was determined based on the mechanical stress analysis results of the ANSYS commercial software (Figure S8) [46,47].

3.3. FCEV network

The FCEV DNNs were constructed for the energy consumption and driving cycle trace NRMSE, which can predict the performance of the vehicle. During this procedure, to exhibit the FC output voltage variation to the two electric motors and consider the sizing of the two electric motors, the constructed DNNs of electric motors were implanted to the FCEV model. The concept of this methodology of FCEV modeling is illustrated in Fig. 7.

3.4. Optimum design problem formulation

To perform the design optimization of the FCEV, the design problem formulation was performed as follows:

Objective function : minimize $f(\mathbf{x})$

Design variables: x_1, x_2, x_3, x_4, x_5

Subjected to

Inequality constraint : $g(\mathbf{x}) \leq 5\%$

Variable bounds : $0.5 \leq x_1 \leq 2,\ 0.7 \leq x_2 \leq 3,$

$4 \leq x_3 \leq 9.13, 0.5 \leq x_4 \leq 2, 0.7 \leq x_5 \leq 2$

Table 7
The fuel economy simulation result from developed FCEV model.

Drive cycle	Fuel economy (km/kWh)	
	Government-certified	FCEV model
City (FTP75)	2.96	2.97
Highway (HWFET)	2.76	2.65
Combined (City×0.55+ Highway×0.45)	2.86	2.83

Here, f denotes the energy consumption of the FCEV, g denotes the trace NRMSE, indicating the difference between the drive cycle and simulation profile. The design variables x_1 and x_2 are the normalized values of the number of armature turns and stack length of the traction motor, respectively. x_3 is the gear ratio of the reduction gear, and x_4 and x_5 are the normalized values of the number of armature turns and stack length of the air compressor motor, respectively. The ranges of the armature turns were determined to satisfy thermal and electrical constraints. The stack length of the traction motor is determined based on the size limit. However, the stack length of the air compressor motor is constrained by the rotor-dynamical reason, i.e., the bending mode frequency [48]. Finally, the range of the reduction gear ratio is determined to satisfy the maximum vehicle speed.

4. Results

4.1. FCEV modeling result

For the developed FCEV model, the mechanical loss curve based on the vehicle speed was adopted, and the losses of other parts losses were considered. In this step, the loss curve was determined to minimize the error in the fuel economy of cities, highways, and combined cycles between the government-certified and simulation values (Table 7).

To investigate the FCEV modeling result, the vehicle simulation was conducted. The purpose of this simulation was to determine whether the components were modeled well, and the drive cycle was adopted to simulate the FCEV under various conditions (Figure S10).

According to the drive cycle shown in Figure S9, the vehicle simulation was conducted, and the results are depicted in Figure S10. The FC voltage variation characteristics according to the FC current are described. The airflow rate and air pressure of the air supply system were simulated, and the corresponding air compressor motor speed and torque were demonstrated.

In addition, the operating points of the traction motor are illustrated in Fig. 8. The blue squares represent the FC voltage constant conditions, and the orange circles represent the FC voltage variation conditions. From this result, it can be confirmed that the effect of FC voltage variation on the FCEV traction system was well-reflected.

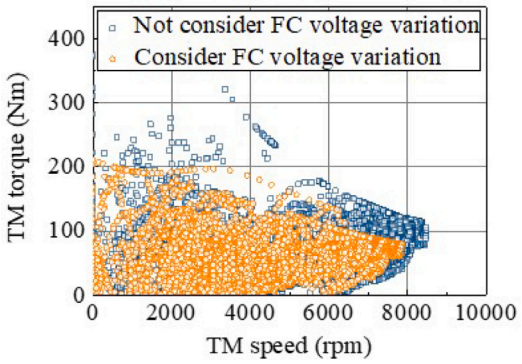

Fig. 8. Operating points of the traction motor.

Table 8
Adaptive layering and sampling results of the electric motors.

Items	Number of		
	Hidden layers	Sampling points	Data sets
Traction motor maximum torque	10	114	2166
Traction motor total loss	18	258	251 136
Air compressor motor maximum torque	31	462	49 564
Air compressor motor total loss	5	60	840

Table 9
Adaptive layering and sampling result for FCEV.

Items	Number of		
	Hidden layers	Sampling points	Data sets
Fuel economy	10	250	250
Trace NRMSE	11	255	255

4.2. DNN construction result

Using the ALS algorithm, as suggested in Section 3.1, the DNNs were constructed. The DNN construction results of the two electric motors are listed in Table 8. The construction profiles based on the ALS algorithm are shown in Figure S12 in supplementary materials.

Moreover, the FCEV DNNs were constructed using the ALS algorithm. This process was performed after the DNNs of two motors were integrated into the FCEV model. The DNN construction results of fuel economy and trace NRMSE are listed in Table 9. The construction profiles based on the ALS algorithm are shown in Figure S13 in supplementary materials.

These results show the effectiveness of the ALS algorithm. All the surrogate models were constructed with different numbers of hidden layers and sampling points. In addition, the range of difference in the number of hidden layers and sampling points is quite broad. This can be interpreted suggested the ALS algorithm helps to train the deep neural network minimizing the computing time and achieving the target accuracy.

4.3. FCEV optimization result

The FCEV optimization was conducted under various drive cycles with various weightings. The target cycles were FTP75, HWFET, and the test cycle, as depicted in Figure S7 of supplementary materials. As listed in Table 10, various weightings are applied and numbered. These various weightings can simulate whether the suggested modeling and optimization method is effective or not because they can act as various optimization problems. For these models, the FCEV optimization was conducted, and the results are listed in Table 11.

Table 10
FCEV optimization models according to the weightings of the drive cycles.

Model number	Weighting		
	FTP75	HWFET	Test cycle
1	1	0	0
2	0	1	0
3	0	0	1
4	1/3	1/3	1/3

From the optimization results, it can be seen that a tendency that the number of armature turns and stack length of the traction motor tended to decrease and the reduction gear ratio tended to increase compared with those of the base model. Thus, we can speculate that, if the combination of the higher reduction gear ratio and the lower torque of the traction motor is adopted, better fuel economy compared to the base model could be achieved. This is consistent with the recent trend in high-speed EV traction motors. In the case of the air compressor motor, there was a tendency, that the number of armature turns and stack length of the traction motor tended to increase compared with those of the base model. And this design direction is advantageous for the motor to produce high torque and disadvantageous for the motor to drive at high speed. Moreover, this condition is advantageous to produce air with low flowrate and high pressure. According to this fact, we can speculate that the FC stack operated more often at a low airflow rate and high air pressure.

Subsequently, graphs that can analyze the optimization results were added as Figure S14 to the Supplementary Materials. The fuel cell efficiency, traction motor loss, and air compressor motor loss were compared with the optimization results for the HWFET, FTP75, and Target driving cycles and the results of the Base Model. In all these results, it can be seen that the fuel cell is well-controlled to operate within a range above a certain efficiency, and the overall efficiency is higher than each optimal model. In addition, it can be seen that the traction motor loss and air compressor motor loss are overall lower in the optimal model, indicating that the optimization has performed well.

5. Conclusion

This study proposed the modeling and optimization methodology for FCEVs. First, in the FCEV modeling process, the traction system of the vehicle, the air supply system for the FC stack, and their performance relationships were considered. In addition, surrogate modeling and optimization processes based on the suggested FCEV model were proposed. In this surrogate modeling process, the ALS algorithm was developed to efficiently construct the DNN. And the effectiveness of the ALS algorithm was confirmed. Therefore, we can conclude that the ALS algorithm can be applied to other meta-modeling processes. Finally, the fuel economy optimizations were conducted for various driving conditions. The optimum sizes of two electric motors and reduction gear ratios were well-designed, and the fuel economy of each driving condition was improved. In addition, it could be monitored that the FC voltage variation to the electric motors was well-considered. Therefore, the usefulness of the DNN-integrated construction methodology was evaluated while modeling the overall system using detailed component models. Overall, it can be concluded that this study suggested an effective modeling methodology and optimization process with reasonable results.

In summary, this research contributes to the advancement of FCEVs by providing a comprehensive modeling and optimization methodology, addressing performance improvements, and utilizing cutting-edge

Table 11
FCEV optimization results according to the models.

Model number	Design result					Fuel economy		
	x_1	x_2	x_3	x_4	x_5	FTP75	HWFET	Test cycle
1	0.85	0.86	9.13	1.76	1.18	3.14 (+6.1%)	2.92 (+5.8%)	2.76 (+3.0%)
2	0.90	0.75	9.13	1.72	1.00	3.10 (+4.7%)	3.00 (+8.7%)	2.79 (+4.1%)
3	0.90	0.82	9.13	1.84	1.32	3.13 (+5.7%)	2.90 (+5.1%)	2.80 (+4.5%)
4	1.00	0.67	8.60	1.28	1.18	3.09 (+4.4%)	2.88 (+4.4%)	2.76 (+3.0%)

techniques such as deep neural networks for design optimization. The practical significance lies in its potential to enhance the efficiency, performance, and commercial viability of FCEVs. Moreover, this suggested methodology can be utilized in various design problems of all the components of FCEVs.

CRediT authorship contribution statement

Dong-Min Kim: Writing – original draft, Visualization, Validation, Software, Methodology, Investigation, Formal analysis, Data curation, Conceptualization. **Kihan Kwon:** Writing – review & editing, Investigation. **Kyoung-Soo Cha:** Writing – review & editing, Software. **Seungjae Min:** Writing – review & editing, Supervision. **Myung-Seop Lim:** Writing – review & editing, Supervision, Project administration.

Declaration of competing interest

The authors declare that they have no known competing financial interests or personal relationships that could have appeared to influence the work reported in this paper.

Data availability

The authors are unable or have chosen not to specify which data has been used.

Appendix A. Supplementary data

Supplementary material related to this article can be found online at https://doi.org/10.1016/j.jpowsour.2024.234401.

References

[1] United Nations Climate Change, The Paris Agreement and NDCs, 2014, https://unfccc.int/process-and-meetings/the-paris-agreement/nationally-determined-contributions-ndcs/nationally-determined-contributions-ndcs. (Accesed on 11 February 2024).

[2] Volvo Cars Global Newsroom, Volvo Cars to be fully electric by 2030, 2024, https://www.media.volvocars.com/global/en-gb/media/pressreleases/{277409}/volvo-cars-to-be-fully-electric-by-2030. (Accesed on 11 February 2024).

[3] D.-Y. Lee, A. Elgowainy, A. Kotz, R. Vijayagopal, J. Marcinkoski, Life-cycle implications of hydrogen fuel cell electric vehicle technology for medium- and heavy-duty trucks, J. Power Sources 393 (2018) 217–229, http://dx.doi.org/10.1016/j.jpowsour.2018.05.012.

[4] L.D. Harvey, Resource implications of alternative strategies for achieving zero greenhouse gas emissions from light-duty vehicles by 2060, Appl. Energy 212 (2018) 663–679, http://dx.doi.org/10.1016/j.apenergy.2017.11.074.

[5] J. Kim, S. Kim, Obstacles to the success of fuel-cell electric vehicles: Are they truly impossible to overcome? IEEE Electrif. Mag. 6 (1) (2018) 48–54, http://dx.doi.org/10.1109/MELE.2017.2784635.

[6] D.-M. Kim, P. Benoliel, D.-K. Kim, T.H. Lee, J.W. Park, J.-P. Hong, Framework development of series hybrid powertrain design for heavy-duty vehicle considering driving conditions, IEEE Trans. Veh. Technol. 68 (7) (2019) 6468–6480, http://dx.doi.org/10.1109/TVT.2019.2914868.

[7] R. Vincent, V. Emmanuel, G. Lauric, G. Laurent, Optimal sizing of an electrical machine using a magnetic circuit model: Application to a hybrid electrical vehicle, IET Electr. Syst. Transp. 6 (1) (2016) 27–33, http://dx.doi.org/10.1049/iet-est.2015.0008.

[8] A.-A. Mamun, Z. Liu, D.M. Rizzo, S. Onori, An integrated design and control optimization framework for hybrid military vehicle using lithium-ion battery and supercapacitor as energy storage devices, IEEE Trans. Transp. Electrification 5 (1) (2019) 239–251, http://dx.doi.org/10.1109/TTE.2018.2869038.

[9] S. Hou, J. Gao, Y. Zhang, M. Chen, J. Shi, H. Chen, A comparison study of battery size optimization and an energy management strategy for FCHEVs based on dynamic programming and convex programming, Int. J. Hydrogen Energy 45 (41) (2020) 21858–21872, http://dx.doi.org/10.1016/j.ijhydene.2020.05.248.

[10] G. Zhang, W. Chen, Q. Li, Modeling, optimization and control of a FC/battery hybrid locomotive based on ADVISOR, Int. J. Hydrogen Energy 42 (29) (2017) 18568–18583, http://dx.doi.org/10.1016/j.ijhydene.2017.04.172.

[11] S.D. Gaikwad, P.C. Ghosh, Sizing of a fuel cell electric vehicle: A pinch analysis-based approach, Int. J. Hydrogen Energy 45 (15) (2020) 8985–8993, http://dx.doi.org/10.1016/j.ijhydene.2020.01.116.

[12] R. Knibbe, D. Harding, J. Burton, E. Cooper, Z. Amir Zadeh, M. Sagulenko, P.A. Meehan, R. Buckley, Optimal battery and hydrogen fuel cell sizing in heavy-haul locomotives, J. Energy Storage 71 (2023) 108090, http://dx.doi.org/10.1016/j.est.2023.108090.

[13] Y. Wang, S.J. Moura, S.G. Advani, A.K. Prasad, Optimization of powerplant component size on board a fuel cell/battery hybrid bus for fuel economy and system durability, Int. J. Hydrogen Energy 44 (33) (2019) 18283–18292, http://dx.doi.org/10.1016/j.ijhydene.2019.05.160.

[14] P. Purnima, S. Jayanti, Optimal sizing of a fuel processor for auxiliary power applications of a fuel cell-powered passenger car, Int. J. Hydrogen Energy 45 (48) (2020) 26005–26019, http://dx.doi.org/10.1016/j.ijhydene.2020.03.127.

[15] K. Kwon, M. Seo, S. Min, Efficient multi-objective optimization of gear ratios and motor torque distribution for electric vehicles with two-motor and two-speed powertrain system, Appl. Energy 259 (2020) 114190, http://dx.doi.org/10.1016/j.apenergy.2019.114190.

[16] X. Hu, Y. Li, C. Lv, Y. Liu, Optimal energy management and sizing of a dual motor-driven electric powertrain, IEEE Trans. Power Electron. 34 (8) (2019) 7489–7501, http://dx.doi.org/10.1109/TPEL.2018.2879225.

[17] K. Li, S. Han, S. Cui, A. Bouscayrol, Sizing of modular cascade machines system for electric vehicles, IEEE Trans. Veh. Technol. 68 (2) (2019) 1278–1287, http://dx.doi.org/10.1109/TVT.2018.2886402.

[18] B. Kabalan, E. Vinot, C. Yuan, R. Trigui, C. Dumand, T.E. Hajji, Efficiency improvement of a series–parallel hybrid electric powertrain by topology modification, IEEE Trans. Veh. Technol. 68 (12) (2019) 11523–11531, http://dx.doi.org/10.1109/TVT.2019.2952190.

[19] E. Carraro, M. Morandin, N. Bianchi, Traction PMASR motor optimization according to a given driving cycle, IEEE Trans. Ind. Appl. 52 (1) (2016) 209–216, http://dx.doi.org/10.1109/TIA.2015.2477479.

[20] B. Dianati, S. Kahourzade, A. Mahmoudi, Optimization of axial-flux induction motors for the application of electric vehicles considering driving cycles, IEEE Trans. Energy Convers. 35 (3) (2020) 1522–1533, http://dx.doi.org/10.1109/TEC.2020.2976625.

[21] K.-S. Cha, D.-M. Kim, Y.-H. Jung, M.-S. Lim, Wound field synchronous motor with hybrid circuit for neighborhood electric vehicle traction improving fuel economy, Appl. Energy 263 (2020) 114618, http://dx.doi.org/10.1016/j.apenergy.2020.114618.

[22] D. Hu, J. Wang, L. Hu, J. Zhou, J. Liu, Research on the damping effect mechanism and optimization of super-high-speed electric air compressors for fuel cell vehicles under the stiffness softening effect, IEEE Access 8 (2020) 179789–179797, http://dx.doi.org/10.1109/ACCESS.2020.3015850.

[23] J.-H. Kim, D.-M. Kim, Y.-H. Jung, M.-S. Lim, Design of ultra-high-speed motor for FCEV air compressor considering mechanical properties of rotor materials, IEEE Trans. Energy Convers. 36 (4) (2021) 2850–2860, http://dx.doi.org/10.1109/TEC.2021.3062646.

[24] D.-M. Kim, J.-H. Kim, S.-G. Lee, M.-R. Park, G.-H. Lee, M.-S. Lim, Estimation method for rotor eddy current loss in ultrahigh-speed surface-mounted permanent magnet synchronous motor, IEEE Trans. Magn. 57 (2) (2021) 1–5, http://dx.doi.org/10.1109/TMAG.2020.3030684.

[25] Y. Zhang, S. Xu, Y. Wan, Performance improvement of centrifugal compressors for fuel cell vehicles using the aerodynamic optimization and data mining methods, Int. J. Hydrogen Energy 45 (19) (2020) 11276–11286, http://dx.doi.org/10.1016/j.ijhydene.2020.02.026.

[26] X. Liang, H. Kang, J. Shen, Z. Li, R. Zeng, Review and analysis of hydrogen recirculation devices for compact vehicular proton exchange membrane fuel cells, J. Power Sources 555 (2023) 232308, http://dx.doi.org/10.1016/j.jpowsour.2022.232308.

[27] M. Tekin, D. Hissel, M.-C. Pera, J.-M. Kauffmann, Energy consumption reduction of a PEM fuel cell motor-compressor group thanks to efficient control laws, J. Power Sources 156 (1) (2006) 57–63, http://dx.doi.org/10.1016/j.jpowsour.2005.08.037.

[28] H. Shao, D. Qiu, L. Peng, P. Yi, X. Lai, In-situ measurement of temperature and humidity distribution in gas channels for commercial-size proton exchange membrane fuel cells, J. Power Sources 412 (2019) 717–724, http://dx.doi.org/10.1016/j.jpowsour.2018.12.008.

[29] J.A. Salva, A. Iranzo, F. Rosa, E. Tapia, Experimental validation of the polarization curve and the temperature distribution in a PEMFC stack using a one dimensional analytical model, Int. J. Hydrogen Energy 41 (45) (2016) 20615–20632, http://dx.doi.org/10.1016/j.ijhydene.2016.09.152.

[30] HYUNDAI MOTORS, NEXO Specifications, 2024, https://www.hyundai.com/kr/en/eco/nexo/specifications. (Accesed on 11 February 2024).

[31] Hyundai Motor Company & Hyundai New Zealand, NEXO Emergency Response Guide, 2024, https://go.hyundai.co.nz/rs/147-PQU-830/images/NEXO%20Emergency%20Response%20Guide%202019.pdf. (Accesed on 11 February 2024).

[32] D.-M. Kim, J.-W. Chin, J.-P. Hong, M.-S. Lim, Performance prediction of surface-mounted permanent magnet synchronous motor based on ring specimen test result, IET Electr. Power Appl. 13 (9) (2019) 1280–1286, http://dx.doi.org/10.1049/iet-epa.2018.5382.

[33] W. Tong, L. Sun, M. Hou, S. Wu, R. Tang, Analytical modeling for rotor eddy current loss of a surface-mounted PMSM with both non-ferromagnetic conductive retaining sleeve and shielding cylinder, IEEE Trans. Energy Convers. Early Access (2021) 1, http://dx.doi.org/10.1109/TEC.2021.3114095.

[34] D.-M. Kim, J.-H. Kim, S.-G. Lee, M.-R. Park, G.-H. Lee, M.-S. Lim, Estimation method for rotor eddy current loss in ultrahigh-speed surface-mounted permanent magnet synchronous motor, IEEE Trans. Magn. 57 (2) (2021) 1–5, http://dx.doi.org/10.1109/TMAG.2020.3030684.

[35] J. Larminie, A. Dicks, Fuel Cell Systems Explained, John Wiley & Sons, Ltd, 2003.

[36] S.N. M., O. Tremblay, L.-A. Dessaint, A generic fuel cell model for the simulation of fuel cell vehicles, in: 2009 IEEE Vehicle Power and Propulsion Conference, 2009, pp. 1722–1729, http://dx.doi.org/10.1109/VPPC.2009.5289692.

[37] F.D. Bianchi, C. Kunusch, C. Ocampo-Martinez, R.S. Sánchez-Peña, A gain-scheduled LPV control for oxygen stoichiometry regulation in PEM fuel cell systems, IEEE Trans. Control Syst. Technol. 22 (5) (2014) 1837–1844, http://dx.doi.org/10.1109/TCST.2013.2288992.

[38] A. Pilloni, A. Pisano, E. Usai, Observer-based air excess ratio control of a PEM fuel cell system via high-order sliding mode, IEEE Trans. Ind. Electron. 62 (8) (2015) 5236–5246, http://dx.doi.org/10.1109/TIE.2015.2412520.

[39] R. Talj, R. Ortega, A. Astolfi, Passivity and robust PI control of the air supply system of a PEM fuel cell model, Automatica 47 (12) (2011) 2554–2561, http://dx.doi.org/10.1016/j.automatica.2011.08.028.

[40] M.P. Klein, J.W. Park, Current distribution measurements in parallel-connected lithium-ion cylindrical cells under non-uniform temperature conditions, J. Electrochem. Soc. 164 (9) (2017) A1893–A1906, http://dx.doi.org/10.1149/2.0011709jes.

[41] Y. Hu, S. Yurkovich, Y. Guezennec, B. Yurkovich, Electro-thermal battery model identification for automotive applications, J. Power Sources 196 (1) (2011) 449–457, http://dx.doi.org/10.1016/j.jpowsour.2010.06.037.

[42] K. Haraldsson, P. Alvfors, Effects of ambient conditions on fuel cell vehicle performance, J. Power Sources 145 (2) (2005) 298–306, http://dx.doi.org/10.1016/j.jpowsour.2004.12.080.

[43] MathWorks, Neural Network Toolbox in MATLAB, 2019.

[44] K. Crombecq, E. Laermans, T. Dhaene, Efficient space-filling and non-collapsing sequential design strategies for simulation-based modeling, European J. Oper. Res. 214 (3) (2011) 683–696, http://dx.doi.org/10.1016/j.ejor.2011.05.032.

[45] M. Johnson, L. Moore, D. Ylvisaker, Minimax and maximin distance designs, J. Statist. Plann. Inference 26 (2) (1990) 131–148, http://dx.doi.org/10.1016/0378-3758(90)90122-B.

[46] D.-M. Kim, Y.-H. Jung, K.-S. Cha, M.-S. Lim, Design of traction motor for mitigating energy consumption of light electric vehicle considering material properties and drive cycles, Int. J. Automot. Technol. 21 (6) (2020) 1391–1399, http://dx.doi.org/10.1007/s12239-020-0131-7.

[47] R.G. Budynas, J.K. Nisbett, J.E. Shigley, Shigley's Mechanical Engineering Design, McGraw-Hill, 2011.

[48] A. Borisavljevic, Limits, Modeling and Design of High-Speed Permanent Magnet Machines, Springer, Berlin, Heidelberg, 2013.